Active whispering-gallery microclock in pulsed-operation mode

Deshui Yu [1], Jingbiao Chen [2,*] and Shougang Zhang [1,3,†]
[1]*National Time Service Center, Chinese Academy of Sciences, Xi'an 710600, China*
[2]*State Key Laboratory of Advanced Optical Communication Systems and Networks, Institute of Quantum Electronics, School of Electronics, Peking University, Beijing, 100871, China*
[3]*University of Chinese Academy of Sciences, Beijing 100049, China*

(Received 13 February 2023; accepted 14 April 2023; published 26 April 2023)

A whispering-gallery-mode microlaser in the bad-cavity limit serves as an active optical clock. In this clock scheme, an ensemble of two-level atoms is trapped in a two-color ring-shaped optical lattice, i.e., Lamb-Dicke regime, and evanescently interacts with an optical microcavity. The microclock is operated in the pulsed mode, where the atoms are periodically pumped into the upper state of the electric-dipole-forbidden clock transition, providing the optical gain. The numerical simulation shows that the fractional frequency instability of the microclock reaches 5×10^{-14} at 10^3 s of averaging, mainly limited by the lattice-induced frequency shifts. This miniature optical clock owns the high integration and can be potentially used to supply the time standard in a photonic network, paving the way towards the on-chip metrology.

DOI: 10.1103/PhysRevA.107.043712

I. INTRODUCTION

Optical atomic clocks have surpassed their microwave counterparts in both frequency stability and accuracy by over two orders of magnitude [1–3], promoting the redefinition of the SI second on an optical reference. The miniaturization of optical clocks is one of the key issues from the viewpoint of out-of-laboratory applications such as satellite-based geopositioning and communication engineering [4,5]. Recently, a transportable optical clock that is fixed in a car trailer showed a frequency stability of $\sim 10^{-15}$ at the averaging time of 1 s and a systematic uncertainty at the 10^{-17} level [6]. The comparison between two transportable optical lattice clocks located in the Tokyo Skytree tower with a 450-m height difference allows for testing the gravitational redshift at the 10^{-5} level [7]. Further shrinking the size of optical clocks down to the chip scale degrades the clock performance because of the cancellation of, for example, the complicated optical systems for laser cooling and trapping of atoms and the prestabilization of local optical oscillators [8]. Nevertheless, such minimized optical references possess the advantages of low cost, less complexity, and small energy consumption and are highly desired for commercial applications. In particular, they can be integrated with nanophotonic waveguides and optical microcombs [9], opening up the possibility of the on-chip optical frequency synthesization [10].

In addition to the usual passive operation, the chip-scale optical clocks may also be operated in the active manner, where a bad-cavity (i.e., the cavity loss rate greatly exceeding the optical gain bandwidth) laser directly serves as a stable optical frequency standard [11]. The underlying mechanism is the substantial suppression of the cavity pulling effect in the bad-cavity limit [12]. In such laser systems, the conventional Fabry-Pérot resonators can be replaced with the whispering-gallery-mode (WGM) microcavities such as microspheres and microtoroids [13–15] that make use of the continuous total reflection at the interface between the dielectric medium and air. These microstructures possess the advantages of high quality factors ($\sim 10^{10}$ [13–15]) and small mode volumes ($\sim 10^{-16}$ m^3 [16]) and have been extensively used in sensing [17–19], nonlinear optics [20], non-Hermitian physics [21–23], and optomechanics [24–26]. Specifically, the strong coupling between trapped atoms and WGM microcavities has been demonstrated in experiments [27–29], showing the potential of implementing the micro-sized light source [30,31].

In this paper, we propose an active optical WGM microclock based on the superradiant emission of ^{87}Sr atoms into a silica microsphere. The atoms are trapped in a two-color ring-shaped optical lattice and interact evanescently with the microsphere. Two lattice wavelengths are respectively close to the blue- and red-detuned magic wavelengths for the ultranarrow-linewidth clock transition. The microclock is operated in the pulsed mode, where the pump and emission processes are separated in time, eliminating the influence of the pump beam on the superradiant radiation. The numerical simulation shows that the fractional Allan deviation of the microclock follows $\sigma_y(\tau) = 1.7 \times 10^{-12}/\sqrt{\tau}$ with the average time τ, primarily limited by the lattice-induced frequency shifts. This active optical microclock can be integrated into a photonic circuit and provide the time standard for the on-chip metrology [32].

II. PHYSICAL MODEL

As shown in Fig. 1(a), an ensemble of ^{87}Sr atoms evanescently interacts with the TE-polarized clockwise ($n_0 = 1$, $l_0 =$

*jbchen@pku.edu.cn
†szhang@ntsc.ac.cn

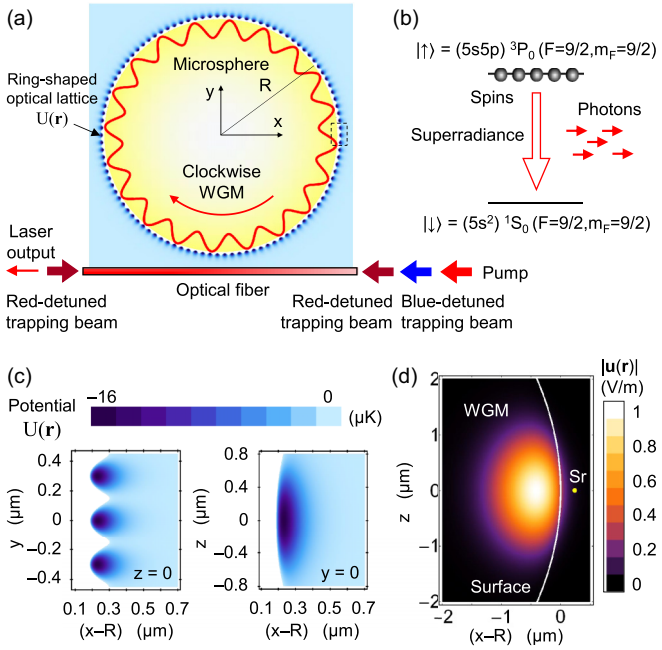

FIG. 1. (a) Schematic diagram of active microclock. A clockwise WGM $\mathbf{u}(\mathbf{r})$ in a microsphere whose radius is $R = 20.3$ μm resonantly interacts with an ensemble of ^{87}Sr spins that are trapped in a two-color ring-shaped optical lattice $U(\mathbf{r})$. All trapping beams, pump light, and clock laser are coupled into or out of the microsphere through a fiber under the critical coupling condition. (b) All spins are initially excited into the upper $|\uparrow\rangle$ state and then collectively emit photons into the microsphere. (c) Section of ring-shaped optical lattice. The potential depth of each lattice site is 16 μK. (d) Evanescent coupling between a spin and the clock WGM $\mathbf{u}(\mathbf{r})$.

$255, m_0 = l_0$) WGM (frequency ω_C) in a silica microsphere whose radius is $R = 20.3$ μm (see Appendixes A and B). Here, we use the radial n, polar l, and azimuthal m numbers to characterize a specific WGM and refer to the (n_0, l_0, m_0) WGM as the clock WGM whose electric field vector is $\mathbf{u}(\mathbf{r})$. Each atom is modeled as a spin-1/2 system, $|\downarrow\rangle = (5s^2)\,^1S_0(F = \frac{9}{2}, m_F = \frac{9}{2})$ and $|\uparrow\rangle = (5s5p)^3P_0(F = \frac{9}{2}, m_F = \frac{9}{2})$ with the clock transition frequency ω_A [see Fig. 1(b)]. The spins are tightly trapped in a two-color ring-shaped optical lattice that is formed around the microsphere [30]. All trapping beams are $\mathbf{e}_z$ polarized and coupled into the microsphere through an optical fiber. Since the resonance wavelengths of WGMs are solely determined by the microsphere's radius R, it is challenging to find other two WGMs (i.e., trapping WGMs) located exactly at the magic wavelengths for the clock transition under the condition that the clock WGM is resonantly coupled to the clock transition. Nonetheless, we may choose the trapping WGMs near the magic wavelengths.

The blue-detuned trapping beam is resonant to the TE-polarized clockwise $(n_b = 1, l_b = 468, m_b = l_b)$ WGM with the resonance wavelength $\lambda_b = 389.974$ nm. Since λ_b is close to the blue-detuned magic wavelength of 389.889 nm for the clock transition [33], the repulsive optical potentials that are exerted by the evanescent field of the (n_b, l_b, m_b) WGM on the spins in $|\downarrow\rangle$ and $|\uparrow\rangle$ approximately have the same profile (see Appendix C). In contrast, two opposite red-detuned trapping beams are resonant to the TE-polarized clockwise and counterclockwise $(n_r = 1, l_r = 218, m_r = \pm 216)$ WGMs, respectively, whose resonance wavelength $\lambda_r = 812.148$ nm is near the red-detuned magic wavelength of 813.428 nm [34]. The superposition of (n_r, l_r, m_r) WGMs forms a standing wave and the attractive optical potentials imposed by the evanescent field on the spins in $|\downarrow\rangle$ and $|\uparrow\rangle$ are approximately the same. Besides optical potentials, the spins in the vicinity of the dielectric surface also experience the attractive van der Waals potentials, which are approximately the same for $|\downarrow\rangle$ and $|\uparrow\rangle$. Due to the difference between the evanescent decay lengths of blue- and red-detuned trapping WGMs, a three-dimensional ring-shaped optical lattice $U(\mathbf{r})$ is attained with the number of lattice sites $2|m_r| = 432$ [see Fig. 1(c)].

Setting the blue-detuned circulating-beam and red-detuned standing-wave powers at 3 and 0.5 W, respectively, the lattice potential depth reaches 16 μK, large enough for trapping ultracold spins [35]. The resultant vibrational frequencies in the radial, polar, and azimuthal directions are $(\Omega_\rho, \Omega_\theta, \Omega_\varphi) = 2\pi \times (105, 11, 110)$ kHz. The corresponding characteristic lengths are computed as $(\xi_\rho, \xi_\theta, \xi_\varphi) = (33, 104, 32)$ nm, where $\xi_{v=\rho,\theta,\varphi} = \sqrt{\hbar/(M\Omega_v)}$ and M is the spin mass. All spins stay in the ground vibrational state $\psi(\mathbf{r})$ and interact with the evanescent field of the clock WGM [see Fig. 1(d)]. The small Lamb-Dicke parameter $\eta = \omega_C \xi_\varphi / c = 0.29$ ensures the recoil-free absorption of pump photons and the emission of clock photons [36]. More details on the ring-shaped optical lattice can be found in Appendix D.

A short pump π pulse, which is resonant to the clock WGM, is applied to excite all spins into $|\uparrow\rangle$, and the superradiant emission occurs subsequently. Due to the directed superradiance of the timed Dicke state [37,38], we neglect the interaction between spins and the counterclockwise $(n_0, l_0, -l_0)$ WGM. The coherent spin-microsphere coupling is described by the Hamiltonian

$$\hat{H}/\hbar = \omega_C \hat{a}^\dagger \hat{a} + \omega_A \hat{J}_z + g(\hat{J}_-^\dagger \hat{a} + \hat{a}^\dagger \hat{J}_-), \tag{1}$$

where $\hat{a}$ and $\hat{a}^\dagger$ are photon annihilation and creation operators of the clock WGM, respectively, and $\hat{J}_- = \sum_j (|\downarrow\rangle\langle\uparrow|)_j$ denotes the lowering operator of the spin ensemble. The subscript j accounts for the jth spin. Three components of the total pseudospin vector $\hat{\mathbf{J}} = \hat{J}_x \mathbf{e}_x + \hat{J}_y \mathbf{e}_y + \hat{J}_z \mathbf{e}_z$ are given by $\hat{J}_x = (\hat{J}_- + \hat{J}_-^\dagger)/2$, $\hat{J}_y = i(\hat{J}_- - \hat{J}_-^\dagger)/2$, and $\hat{J}_z = i(\hat{J}_y \hat{J}_x - \hat{J}_x \hat{J}_y)$. The spin-microsphere coupling strength takes the form

$$g = \frac{\mu}{\hbar}\sqrt{\frac{\hbar\omega_C}{2\varepsilon_0 V}} \int [\mathbf{u}(\mathbf{r})\mathbf{e}_z]\psi(\mathbf{r}) d\mathbf{r}, \tag{2}$$

with the dipole matrix element μ of the clock transition. The microcavity mode volume

$$V = \frac{\int \epsilon(|\mathbf{r}|)|\mathbf{u}(\mathbf{r})|^2 d\mathbf{r}}{\max[\epsilon(|\mathbf{r}|)|\mathbf{u}(\mathbf{r})|^2]}, \tag{3}$$

approximates 2×10^{-17} m^3, which is, for example, six orders of magnitude smaller than that of the Fabry-Pérot cavity in [39], resulting in $g = 2\pi \times 0.3$ kHz. Here, $\epsilon(|\mathbf{r}| < R)$ denotes the relative permittivity of the microsphere while $\epsilon(|\mathbf{r}| > R) = 1$.

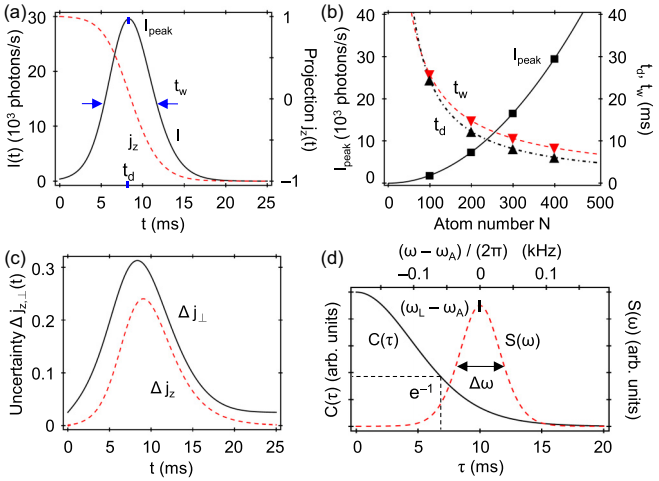

FIG. 2. (a) Superradiant pulse $I(t)$ and single-spin population inversion $j_z(t)$ with the spin number $N = 400$. (b) Peak emission rate I_{peak}, delay time t_d, and pulse duration t_w versus N. Symbols: numerical simulation. Squares represent I_{peak}, up triangles are assigned to t_d, and down triangles correspond to t_w. Lines: curve fitting. Solid line: I_{peak}. Dash-dotted line: t_d. Dashed line: t_w. (c) Uncertainties $\Delta j_{z,\perp}(t)$ with $N = 400$. (d) Correlation function $C(\tau)$ and spectrum $S(\omega)$ with $N = 400$. For all curves and symbols, the spins resonantly interact with the microsphere, $\omega_C = \omega_A$.

The dissipative dynamics of the coupled system is governed by the master equation [40]

$$d\hat{\rho}/dt = -i[\hat{H}/\hbar, \hat{\rho}] + \mathcal{D}(\hat{\rho}), \tag{4}$$

of the spin-microcavity density matrix $\hat{\rho}(t)$ with the Lindblad operator

$$\mathcal{D}(\hat{\rho}) = \kappa(\hat{a}\hat{\rho}\hat{a}^{\dagger} - \hat{a}^{\dagger}\hat{a}\hat{\rho}/2 - \hat{\rho}\hat{a}^{\dagger}\hat{a}/2). \tag{5}$$

Here, we omit the spontaneous decay of spins since the lifetime of $|\uparrow\rangle$ is over 10^2 s, much longer than the clock cycle time (see below). The extra dephasing sources such as collisional (density) shifts and high-order ac Stark shifts can be substantially suppressed using the methods of shallow optical lattices and operational magic intensities [41–44], and are thereby negligible. At the critical fiber-microsphere coupling point [45], the linewidth of the clock WGM is $\kappa = 2\pi \times 1.2$ MHz (see Appendix B). In the adiabatic limit $\kappa \gg g$, the photon operator may be approximately expressed as $\hat{a} = -ig\hat{J}_-/(\kappa/2 + i\Delta)$ with the detuning $\Delta = \omega_C - \omega_A$ [46]. The expectation value of an arbitrary operator $\hat{O}$ is given by $\langle\hat{O}(t)\rangle = \text{Tr}[\hat{\rho}(t)\hat{O}]$. We explore the superradiance by directly solving the master equation, rather than using the mean-field method. Due to the absence of inhomogeneous sources, the maximally symmetric Dickes states [47,48] can be chosen as the basis states of spins.

III. SUPERRADIANCE

Figure 2(a) depicts an example of the time evolution of the photon emission rate $I(t) = (\kappa/2)\langle\hat{a}^{\dagger}(t)\hat{a}(t)\rangle$. It is seen that $I(t)$ presents an asymmetric pulse shape and can be characterized by the peak emission rate I_{peak}, the delay time t_d of the peak, and the full width at half maximum duration t_w. According to [49], we predict $I_{\text{peak}} = c_{\text{peak}}N^2g^2/\kappa$, $t_d = (c_d\kappa \ln N)/(Ng^2)$, and $t_w = c_w\kappa/(Ng^2)$ with the spin number N and the dimensionless factors $c_{\text{peak}} = 0.39$, $c_d = 0.26$, and $c_w = 1.2$ determined by the curve fitting [see Fig. 2(b)]. Unlike [49], in which the atom number exceeds 10^5, I_{peak} does not show a threshold behavior because of the absence of the atomic decoherence or atom loss in our relatively small system. Additionally, the analysis in [49] is based upon the mean-field theory, where the quantum fluctuations of the spins are omitted. In contrast, we directly solve the master equation without using the mean-field approximation. Both reasons contribute to the difference between $(c_{\text{peak}}, c_d, c_w)$ obtained in this work and the ones in [49].

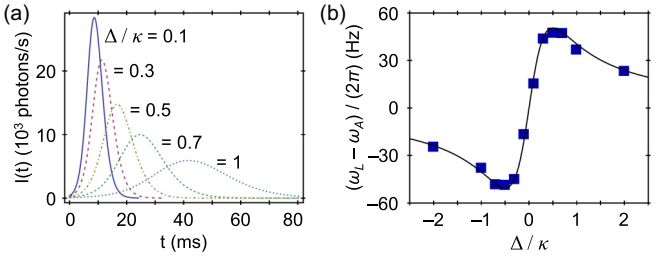

FIG. 3. (a) Superradiant pulses $I(t)$ with different detunings Δ. Here, Δ is introduced by varying the clock WGM frequency ω_C. (b) Frequency shift versus Δ. Symbols: numerical simulation. Lines: curve fitting. For all curves and symbols, the spin number is $N = 400$.

Following the photon emission, the single-spin population inversion $j_z(t) = \langle\hat{J}_z(t)\rangle/J$ exhibits a damping behavior that is maximized at t_d. Here, $J = N/2$ denotes the total angular momentum quantum number. In contrast, $j_{\perp}(t) = \langle\hat{J}_{\perp}(t)\rangle/J$ of an arbitrary transverse vector $\hat{J}_{\perp}\mathbf{e}_{\perp}$ with $\mathbf{e}_{\perp}\mathbf{e}_z = 0$ stays at zero. The uncertainty of $\hat{J}_{\alpha=z,\perp}/J$ is given by $\Delta j_{\alpha}(t) = \sqrt{\langle\hat{J}_{\alpha}^2(t)\rangle - \langle\hat{J}_{\alpha}(t)\rangle^2}/J$. In spite of $\Delta j_z(0) = 0$, the initial nonzero quantum fluctuations $\Delta j_{\perp}(0) = 1/\sqrt{N}$ turn on the superradiant emission. At t_d, $\Delta j_{\perp}(t)$ reaches its maximum, boosting the decay of the spin ensemble [see Fig. 2(c)]. It should be noted that $\Delta j_{z,\perp}$ are omitted in the mean-field approximation [49].

The autocorrelation function $C(\tau) = \int\langle\hat{a}^{\dagger}(t+\tau)\hat{a}(t)\rangle dt$ of the superradiant pulse is computed using the quantum regression theorem [17]. We find that $C(\tau)$ primarily follows a Gaussian damping profile with a characteristic $1/e$ decay time close to t_w [see Fig. 2(d)]. This coherence time is multiple orders of magnitude longer than the cold-cavity lifetime κ^{-1}. Indeed, it arises from the fact that the long-lived quantum memory of the collective spin polarization maintains the temporal coherence of the superradiant emission [50]. The power spectral density of the superradiant pulse is given by the Fourier transform $S(\omega) = \int C(\tau)e^{-i\omega\tau}d\tau$, of whom the full width at half maximum $\Delta\omega$ approximates $\sim(4\sqrt{\ln 2})t_w^{-1}$.

The profile of the superradiant emission depends strongly on the detuning Δ. As illustrated in Fig. 3(a), when $|\Delta|$ grows the peak emission rate I_{peak} decreases and the width t_w is broadened. To interpret this, we rewrite the dissipative term in the master equation as

$$\mathcal{D}(\hat{\rho}) = \Gamma(\hat{J}_-\hat{\rho}\hat{J}_+ - \hat{J}_+\hat{J}_-\hat{\rho}/2 - \hat{\rho}\hat{J}_+\hat{J}_-/2), \tag{6}$$

where the collective decay rate $\Gamma = g^2\kappa/(\kappa^2/4 + \Delta^2)$ declines as $|\Delta|$ is increased. In addition, the central frequency ω_L of the superradiant spectrum $S(\omega)$ presents a dispersion behavior around $|\Delta| \sim 0$, $(\omega_L - \omega_A) \propto g^2\Delta/(\kappa^2/4 + \Delta^2)$ [see Fig. 3(b)]. Actually, this frequency shift originates from the long-range exchange interactions between spins mediated by the microcavity [46]. The resonant spin-microsphere coupling leads to $\omega_L = \omega_A$. Since the system is operated in the bad-cavity regime $\kappa \gg g$, the shift $|\omega_L - \omega_A|$ is well below κ, that is, the cavity pulling effect is substantially suppressed.

IV. UNCERTAINTIES

The superradiant emission is subject to various uncertainties. To eliminate the clock frequency shifts caused by the long-range virtual-photon-mediated interactions between spins [51], the number N of lattice-trapped spins should be small enough that each lattice site is occupied by, at most, one spin. The ensemble of spins is released from the optical lattice after collectively emitting photons and a new spin ensemble is then prepared (i.e., cooling and trapping) and excited into $|\uparrow\rangle$. Thus, N varies for different ensembles. We set the average value of N to be $\bar{N} = 400$ with a standard deviation $\sigma_N = 40$. The nonzero σ_N affects I_{peak}, $t_{d,w}$, and $\Delta\omega$, rather than shifting the clock transition frequency ω_A.

It is essential to consider the lattice-induced light shifts of the clock transition, although the trapping beam wavelengths $\lambda_{b,r}$ are respectively apart from the blue- and red-detuned magic wavelengths by small amounts. At lattice sites, the local evanescent intensities of blue-detuned circulating and red-detuned standing waves are 11 and 37 kW/cm^2, respectively, leading to the corresponding light shifts of 2.4 kHz and -1.9 kHz. Assuming the uncertainties of the trapping-beam intensities to be $\sim$10%, the resultant uncertainty of ω_A is 0.4 kHz. In addition, the small difference of the van der Waals potentials exerting on the spin in $|\downarrow\rangle$ and $|\uparrow\rangle$ leads to an extra clock frequency shift of 1.5 kHz. The spatial distribution uncertainty ξ_ρ introduces an extra uncertainty of 0.3 kHz to ω_A. Therefore, the total uncertainty of ω_A induced by the ring-shaped optical lattice is $\delta\omega_A = 2\pi \times 0.7$ kHz, which actually accounts for the optical gain bandwidth.

In addition, various environmental noises such as ground vibrations and temperature fluctuations disturb the clock WGM frequency ω_C. The fundamental stability of ω_C is placed by the thermorefractive noise, where the thermal fluctuations cause the variations of the refractive index in the dielectric microsphere [52]. The corresponding Allan deviation is computed as $\sigma_{C,y}^{\text{TR}}(\tau) = 6.6 \times 10^{-13}/\sqrt{\tau}$ with the average time τ. Indeed, the practical frequency noise spectrum of ω_C follows

$$S_C(f) = \int \langle \omega_C(t+\tau)\omega_C(t)\rangle e^{-i2\pi f\tau} d\tau = h_{C,0}f^0 + h_{C,-2}f^{-2}, \tag{7}$$

with $h_{C,0} = 2\kappa/\omega_C^2 = 2.0 \times 10^{-24}$ s and the typical value $h_{C,-2} = 2.0 \times 10^{-22}$ s^{-1} [18]. The white frequency noise component ($\propto f^0$) governs the high-f regime and the corresponding Allan deviation is given by $\sigma_{C,y}^{\text{WT}}(\tau) = \sqrt{h_{C,0}/(2\tau)} = 1.0 \times 10^{-12}/\sqrt{\tau}$. In contrast, the brown noise component ($\propto f^{-2}$) arises from the linear drift of ω_C and dominates the low-f regime. The corresponding Allan deviation is expressed as $\sigma_{C,y}^{\text{BN}}(\tau) = \sqrt{2\pi^2 h_{C,-2}\tau/3} = 3.6 \times 10^{-11}\sqrt{\tau}$. Both $\sigma_{C,y}^{\text{WT}}(\tau)$ and $\sigma_{C,y}^{\text{BN}}(\tau)$ are above $\sigma_{C,y}^{\text{TR}}(\tau)$ (see Fig. 4). Nevertheless, as we will see below, the WGM frequency fluctuations hardly influence the stability of the central frequency ω_L of the superradiant emission in the bad-cavity limit.

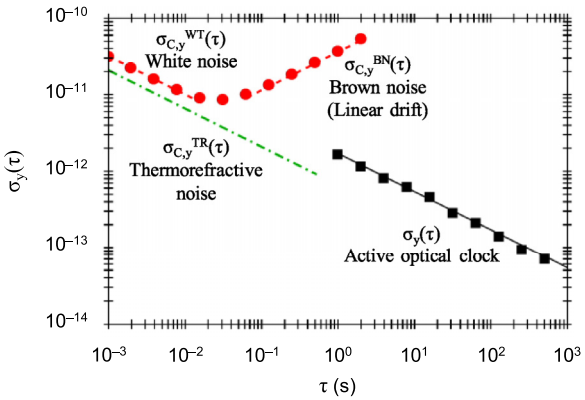

FIG. 4. Fractional Allan deviation $\sigma_y(\tau)$ of the WGM microclock with the clock cycle $T_c = 1$ s. Symbols: numerical results. Circles represent the frequency stability of the WGM microcavity under the perturbation of white frequency noise $\sigma_{C,y}^{\text{WT}}(\tau)$ and linear-drift-induced brown noise $\sigma_{C,y}^{\text{BN}}(\tau)$. Squares correspond to the frequency stability of the active optical clock. Lines: curve fitting. Solid line: frequency stability of the active optical clock. Dashed lines: typical white-noise-limited $\sigma_{C,y}^{\text{WT}}(\tau)$ and linear-drift-limited $\sigma_{C,y}^{\text{BN}}(\tau)$ stabilities of a practical WGM microcavity. Dash-dotted line: thermorefractive-noise-limited stability $\sigma_{C,y}^{\text{TR}}(\tau)$ of the WGM microcavity.

V. CLOCK OPERATION

We now consider the microclock running in the pulsed mode. The clock cycle, which includes the preparation (i.e., laser cooling and trapping) and excitation of an ensemble of spins and the detection of the superradiant emission, is repeated continuously (see Appendix E). One may numerically simulate the clock operation as follows: For each cycle with a duration T_c, the spin number N is generated according to the gaussian distribution with the mean $\bar{N}$ and the standard deviation σ_N. The light shift of ω_A is produced according to the Gaussian distribution with the mean of 2 kHz and the standard deviation $\delta\omega_A$. In addition, the time sequence of the WGM frequency ω_C is created based on the noise spectrum $S_C(f)$ using the digital filtering method [53]. After simulating each superradiant pulse, the corresponding spectrum $S(\omega)$ is computed through the quantum regression theorem and the central frequency ω_L is determined accordingly. Finally, the Allan deviation $\sigma_y(\tau)$ of ω_L is evaluated, where the average time τ must be the integer multiple of T_c. Within T_c, the superradiant emission measurement time is set to be 0.1 s, greatly exceeding the typical pulse width t_w, while the rest duration accounts for the preparation and excitation of a new spin ensemble.

The simulation results are plotted in Fig. 4. Since the optical gain bandwidth $\delta\omega_A$ well surpasses the cavity pulling effect in the bad-cavity limit, the fractional frequency instability of the microclock is dominated by the total uncertainty of lattice-induced light shifts. The curve fitting illustrates

$$\sigma_y(\tau) = \frac{\delta\omega_A}{\omega_A}\sqrt{\frac{T_c}{\tau}} = (1.7\times 10^{-12})\sqrt{\frac{T_c}{\tau}}. \tag{8}$$

Reducing the cycle duration T_c enhances the frequency stability. However, the preparation and excitation of spins restrict a strong suppression of T_c. We choose the typical value $T_c = 1$ s and obtain the frequency stability of 5×10^{-14} at $\tau = 10^3$ s, encouragingly close to that of the recently demonstrated chip-scale optical clock [8].

In practice, the stability $\sigma_y(\tau)$ can be derived from the heterodyne beat measurement between the active microclock and a highly stable reference laser [11]. A number of technical noises potentially degrade the frequency comparison. In our active system, each spin emits only one photon per clock cycle. At the critical coupling point [45], half of the intracavity photons can be collected by the photodetector. The corresponding photon shot noise leads to the signal-to-noise ratio $\mathrm{SNR} = \sqrt{\bar{N}/2} \approx 14$ of the heterodyne detection, high enough to suppress the relevant influence on $\sigma_y(\tau)$. Additionally, the Dicke effect caused by the relatively large dead time (occupying 90 percent of the clock cycle) converts the high-frequency noise of the reference laser down to low Fourier frequencies [54]. Following the method introduced in [11], the relevant contribution is estimated to be of the order of 10^{-16} at $\tau = 1$ s of averaging, negligible to $\sigma_y(\tau)$.

VI. CONCLUSION

In summary, we proposed an active optical microclock based on the WGM microcavity. The cavity pulling effect is considerably suppressed in the bad-cavity limit. In the pulsed operation, the pump and emission processes are separated in time, eliminating the pump-beam-induced light shifts. The frequency stability of the microclock follows $\sigma_y(\tau) = 1.7\times 10^{-12}/\sqrt{\tau}$, primarily limited by the lattice-induced light shifts. The trapping beam wavelengths do not satisfy the magic-wavelength condition, resulting in light shifts much larger than that of conventional optical lattice clocks. The different van der Waals potentials exerted on the spin in $|\uparrow\rangle$ and $|\downarrow\rangle$ add an extra shift to the clock transition. The substantial reduction of these light shifts relies on the appropriate microcavity design. Engineering microclocks, frequency microcombs, and waveguides on a photonic chip potentially allows for the on-chip optical frequency comparison and synchronization.

ACKNOWLEDGMENTS

D. Y. thanks the funding provided by National Time Service Center, China (Grant No. E239SC11).

APPENDIX A: WHISPERING-GALLERY MODES IN MICROSPHERE

The mechanism of optical WGMs originates from the continuous total internal reflection of light waves at the interface between the microcavity and its surrounding medium. The isotropic dielectric microsphere has a relative permittivity ϵ_i higher than that of the outside-sphere region ϵ_o. In spherical coordinates (ρ,θ,φ), the rigorous solutions of TE-polarized WGMs that are allowed to exist in the microsphere are expressed as [17]

$$\mathbf{E}^{(\mathrm{i})}_{n,l,m}(\mathbf{r}) = A^{(\mathrm{i})}_{n,l,m}\frac{\psi_l(k_\mathrm{i}\rho)}{k_\mathrm{i}\rho}\mathbf{X}_{l,m}(\theta,\varphi), \quad \rho < R, \tag{A1a}$$

$$\mathbf{E}^{(\mathrm{o})}_{n,l,m}(\mathbf{r}) = A^{(\mathrm{o})}_{n,l,m}\frac{\xi_l(k_\mathrm{o}\rho)}{k_\mathrm{o}\rho}\mathbf{X}_{l,m}(\theta,\varphi), \quad \rho > R, \tag{A1b}$$

with the amplitudes $A^{(\mathrm{i})}_{n,l,m}$ and $A^{(\mathrm{o})}_{n,l,m}$ and the intracavity (outside-cavity) wave number $k_\mathrm{i} = \sqrt{\epsilon_\mathrm{i}}\omega/c$ ($k_\mathrm{o} = \sqrt{\epsilon_\mathrm{o}}\omega/c$). A specific WGM is characterized by the radial $n \geqslant 1$, polar l, and azimuthal m numbers. The fundamental WGMs correspond to $(n = 1, l, m = \pm l)$. WGMs with $m > 0$ ($m < 0$) circulate in the clockwise (counterclockwise) direction. In above equations, we defined the Ricatti-Bessel $\psi_l(z) = z j_l(z)$ and $\xi_l(z) = \psi_l(z) + iz n_l(z)$ functions with the spherical Bessel functions $j_l(z)$ and $n_l(z)$. The vector spherical harmonics takes the form

$$\mathbf{X}_{l,m}(\theta,\varphi) = \left[\nabla Y^m_l(\theta,\varphi)\right]\times\mathbf{r}, \tag{A2}$$

with the spherical harmonic function $Y^m_l(\theta,\varphi)$. The boundary conditions lead to

$$A^{(\mathrm{i})}_{n,l,m}\psi'_l(k_\mathrm{i}R) = A^{(\mathrm{o})}_{n,l,m}\xi'_l(k_\mathrm{o}R), \tag{A3a}$$

$$k_\mathrm{o}A^{(\mathrm{i})}_{n,l,m}\psi_l(k_\mathrm{i}R) = k_\mathrm{i}A^{(\mathrm{o})}_{n,l,m}\xi_l(k_\mathrm{o}R), \tag{A3b}$$

from which one may derive the resonance frequency ω and further compute the electric-field profile of the (n,l,m) WGM. According to [55], the WGM frequency ω depends on (n,l) and can be approximately evaluated by the following asymptotic formula:

$$\omega_{n,l} = \frac{c}{R\sqrt{\epsilon_\mathrm{i}}}\left[\nu + \frac{\alpha_n}{2^{1/3}}\nu^{1/3} - \sqrt{\frac{\epsilon_\mathrm{i}}{\epsilon_\mathrm{i}-\epsilon_\mathrm{o}}} + \frac{3}{10}\frac{\alpha_n^2}{2^{2/3}}\nu^{-1/3} - \frac{1}{3}\left(\frac{\epsilon_\mathrm{i}}{\epsilon_\mathrm{i}-\epsilon_\mathrm{o}}\right)^{3/2}\frac{\alpha_n}{2^{1/3}}\nu^{-2/3} + O(\nu^{-1})\right], \tag{A4}$$

with $\nu = l + 1/2$ and the nth root α_n of the Airy function $\mathrm{Ai}(-\alpha)$. For silica, its dispersion equation is given by [56]

$$\epsilon_\mathrm{i} = 1 + \frac{0.6961663\times\lambda^2}{\lambda^2 - 0.0684043^2} + \frac{0.4079426\times\lambda^2}{\lambda^2 - 0.1162414^2} + \frac{0.8974794\times\lambda^2}{\lambda^2 - 9.896161^2}, \tag{A5}$$

where the wavelength λ is in units of μm. Substituting $R = 20.3$ μm, Eq. (A5), and $\epsilon_\mathrm{o} = 1$ into Eq. (A4), we find the following WGM resonance wavelengths $\lambda = 2\pi c/\omega$:

$\lambda_C = 698.446$ nm for $(n_0 = 1, l_0 = 255, m_0 = 255)$,

$\lambda_b = 389.974$ nm for $(n_b = 1, l_b = 468, m_b = 468)$,

$\lambda_r = 812.148$ nm for $(n_r = 1, l_r = 218, m_r = \pm 216)$.

APPENDIX B: QUALITY FACTOR OF CLOCK WGM

Various optical loss mechanisms influence the quality factor Q of the microcavity. (1) The radiation loss is attributed to the fact that a portion of light leaks out of the microsphere each time when the beam hits on the microsphere's surface. The relevant quality factor may be evaluated by

$$Q_{\rm rad} = \frac{2l+1}{4}\sqrt{\frac{\epsilon_{\rm i}-1}{\epsilon_{\rm i}}}\exp\left[(2l+1)(\beta_{n,l}-\tanh\beta_{n,l})\right], \tag{B1}$$

with the shorthand

$$\beta_{n,l} = \cosh^{-1}\left\{\sqrt{\epsilon_{\rm i}}\left[1+\frac{2}{2l+1}\left(\alpha_n\left(\frac{2l+1}{4}\right)^{1/3} - \sqrt{\frac{\epsilon_{\rm i}}{\epsilon_{\rm i}-1}}\right)\right]^{-1}\right\}. \tag{B2}$$

(2) When the light wavelength λ is located outside the transparency window of the cavity material, the light beam suffers from a strong attenuation when circulating inside the microsphere. The material-loss-limited quality factor $Q_{\rm mat}$ takes the form

$$Q_{\rm mat} = \frac{2\pi}{\lambda}\frac{\sqrt{\epsilon_{\rm i}}}{\alpha_{\rm mat}}, \tag{B3}$$

with the attenuation coefficient $\alpha_{\rm mat}$. Generally, $\alpha_{\rm mat}$ of silica is composed of Rayleigh scattering and the material absorption (mainly in the infrared regime). (3) The imperfect fabrication techniques inevitably lead to a surface roughness of the microsphere. Thus, the light traveling at the microsphere's surface experiences a discontinuity in refractive index. The surface-roughness-limited quality factor $Q_{\rm ss}$ may be expressed as [14]

$$Q_{\rm ss} = \frac{3\sqrt{\epsilon_{\rm i}}}{4\pi^2}\left(\frac{\epsilon_{\rm i}}{\epsilon_{\rm i}-1}\right)^2\frac{\lambda^3\sqrt{2R\lambda}}{\sigma^2 B^2}, \tag{B4}$$

with the standard deviation σ and the spatial correlation length B of the surface roughness of the microsphere. (4) After the fabrication, the hemosorption of the atmospheric water can form a layer of OH groups upon the microsphere's surface. The adsorbed water may cause the extra optical loss and the relevant quality factor is estimated by [14]

$$Q_{\rm sa} = \sqrt{\frac{\pi R}{16 n_{\rm wat}^3\lambda}}\frac{1}{\delta\beta}, \tag{B5}$$

with the refractive index $n_{\rm wat}$, thickness δ, and absorption coefficient β of the water layer.

We are interested in the quality factor of the clock (n_0, l_0, m_0) WGM that is used for the clock operation. Different quality factor components are listed in Table I. The intrinsic quality factor is evaluated as

$$Q_0 = \left(Q_{\rm rad}^{-1}+Q_{\rm mat}^{-1}+Q_{\rm ss}^{-1}+Q_{\rm sa}^{-1}\right)^{-1} \approx 7.3\times 10^8. \tag{B6}$$

In addition, the fiber-microcavity coupling introduces an extra cavity loss and the relevant quality factor is Q_c. The total quality factor of the clock WGM is then given by $Q = (Q_0^{-1} + Q_c^{-1})^{-1}$. Typically, the fiber-microcavity coupler is operated at the so-called critical coupling point [45], $Q_0 = Q_c$, and hence one has the total cavity loss rate $\kappa = \omega/Q = 2\pi \times 1.2$ MHz.

TABLE I. Different quality factor components of the clock (n_0, l_0, m_0) WGM.

Radiation-loss-induced $Q_{\rm rad}$	7.7×10^{38}
Material-loss-induced $Q_{\rm mat}$ [a]	1.5×10^{10}
Surface-scattering-induced $Q_{\rm ss}$ [b]	7.3×10^{8}
Surface-absorption-induced $Q_{\rm sa}$ [c]	1.3×10^{10}
Intrinsic quality factor Q_0	7.3×10^{8}
Total quality factor Q [d]	3.6×10^{8}

[a] At $\lambda = 698$ nm, $\alpha_{\rm mat}$ approximates 3.7 dB/km [57].
[b] In the experiment, σ is 2 nm and B is 5 nm.
[c] In the experiment, δ approximates 0.2 nm.
[d] At the critical coupling point, the coupling quality factor is equal to Q_0.

APPENDIX C: AC STARK SHIFTS AND VAN DER WAALS POTENTIALS

To the second-order approximation, the ac Stark shift $\Delta\nu$ of the clock transition induced by a far-detuned light field (intensity I_0 and wavelength λ) is expressed as [58]

$$h\Delta\nu(\lambda) = -\frac{c\mu_0 I_0}{2}[\alpha_{|\uparrow\rangle}(\lambda) - \alpha_{|\downarrow\rangle}(\lambda)], \tag{C1}$$

where $\alpha_{|u\rangle=|\uparrow\rangle,|\downarrow\rangle}$ corresponds to the dynamic polarizability of the $|u\rangle$ spin. One may compute $\alpha_{|u\rangle}(\lambda)$ by using the data listed in [59]. The light shift $\Delta\nu$ vanishes at the blue-detuned magic wavelength of 389.889 nm [33] and the red-detuned magic wavelength of 813.428 nm [34]. Around magic wavelengths, the rate of change of $\Delta\nu$ with respect to λ is $(d\Delta\nu/d\lambda)_{\lambda=389.889\ \rm nm} = 2.67$ kHz/nm and $(d\Delta\nu/d\lambda)_{\lambda=813.428\ \rm nm} = 39.5$ Hz/nm, where we set $I_0 = 1$ kW/cm^2. Thus, we obtain $\Delta\nu(\lambda_b) = 226$ Hz and $\Delta\nu(\lambda_r) = -50$ Hz. It was found that the relative difference between $\alpha_{|\uparrow\rangle}$ and $\alpha_{|\downarrow\rangle}$ at λ_b is about 1%. Approximately, we may treat $\alpha_{|\uparrow\rangle} \sim \alpha_b \equiv \alpha_{|\downarrow\rangle} = -455$ a.u. when considering the optical potential produced by the blue-detuned (n_b, l_b, m_b) WGM. Similarly, the relative difference between $\alpha_{|\uparrow\rangle}$ and $\alpha_{|\downarrow\rangle}$ at λ_r is less than 2%. We approximately treat $\alpha_{|\uparrow\rangle} \sim \alpha_r \equiv \alpha_{|\downarrow\rangle} = 278$ a.u. when considering the standing-wave optical potential produced by the red-detuned $(n_r, l_r, \pm m_r)$ WGMs.

Besides optical potentials (i.e., ac Stark shifts), the spin in the vicinity of the dielectric surface with a distance d also experiences the van der Walls potential [60]

$$U_{\rm vdW}(|u\rangle = |\uparrow\rangle, |\downarrow\rangle) = -\frac{C_3(|u\rangle)}{d^3}, \tag{C2}$$

with the coefficient $C_3(|u\rangle)$ for the spin in $|u\rangle$,

$$C_3(|u\rangle) = \frac{\hbar}{16\pi^2\varepsilon_0}\int_0^\infty \alpha_{|u\rangle}(iz)\frac{\epsilon(iz)-1}{\epsilon(iz)+1}dz. \tag{C3}$$

The relative permittivity function ϵ is given by Eq. (A5). The relative difference between $C_3(|\uparrow\rangle)$ and $C_3(|\downarrow\rangle)$ is less than 3% and one may treat $C_3(|\uparrow\rangle) \sim C_3 \equiv C_3(|\downarrow\rangle) = 4.8\times 10^{-49}$ J m^3.

APPENDIX D: RING-SHAPED OPTICAL LATTICE

In spherical coordinates (ρ, θ, φ), the total potential exerted on a spin in the vicinity of microsphere is written as [30]

$$U_{\rm tot}(\mathbf{r}) = U_b(\mathbf{r}) + U_r(\mathbf{r}) - \frac{C_3}{(\rho - R)^3}, \tag{D1}$$

with the blue-detuned (replusive) $U_b(\mathbf{r})$ and red-detuned (attractive) $U_r(\mathbf{r})$ optical potentials

$$U_b(\mathbf{r}) = -\frac{\alpha_b}{4}\left|\mathbf{E}^{(\rm o)}_{n_b,l_b,m_b}(\mathbf{r})\right|^2, \tag{D2a}$$

$$U_r(\mathbf{r}) = -\frac{\alpha_r}{4}\left|\mathbf{E}^{(\rm o)}_{n_r,l_r,m_r}(\mathbf{r}) + \mathbf{E}^{(\rm o)}_{n_r,l_r,-m_r}(\mathbf{r})\right|^2. \tag{D2b}$$

The trapping beam powers are given by

$$P_b = \frac{c\varepsilon_0}{2}\int \sqrt{\epsilon(\rho)}\left|\mathbf{E}^{(\rm i/o)}_{n_b,l_b,m_b}(\mathbf{r})\right|^2 \rho d\rho \sin\theta d\theta d\theta, \tag{D3a}$$

$$P_r = \frac{c\varepsilon_0}{2}\int \sqrt{\epsilon(\rho)}\left|\mathbf{E}^{(\rm i/o)}_{n_r,l_r,m_r}(\mathbf{r}) + \mathbf{E}^{(\rm i/o)}_{n_r,l_r,-m_r}(\mathbf{r})\right|^2 \times \rho d\rho \sin\theta d\theta, \tag{D3b}$$

with the spatial distribution of the relative permittivity $\epsilon(\rho < R) = \epsilon_{\rm i}$ and $\epsilon(\rho > R) = \epsilon_{\rm o}$. We focus on the lattice site located at $(\rho_0, \theta = \pi/2, \varphi = 0)$ and consider the vibrational states of the spin (mass M) moving in $U_{\rm tot}(\mathbf{r})$. The value of ρ_0 will be determined later. The corresponding Schrödinger equation takes the form

$$\left[-\frac{\hbar^2}{2M}\left(\frac{\partial^2}{\partial\rho^2} + \frac{2}{\rho}\frac{\partial}{\partial\rho} + \frac{1}{\rho^2\sin\theta}\frac{\partial}{\partial\theta}\sin\theta\frac{\partial}{\partial\theta} + \frac{1}{\rho^2\sin^2\theta}\frac{\partial^2}{\partial\varphi^2}\right) + U_{\rm tot}(\mathbf{r})\right]\psi(\mathbf{r}) = E\psi(\mathbf{r}), \tag{D4}$$

with the eigenfunction $\psi(\mathbf{r})$ and the eigenvalue E. Since the WGMs are tightly confined near the equator of the microsphere, i.e., $\theta \sim \pi/2$, the harmonic vector $\mathbf{X}_{l,m}(\theta, \varphi)$ is simplified as

$$\mathbf{X}_{l,m}(\theta,\varphi) \approx \Theta_{l,m}(\theta)\mathbf{e}_z = \frac{(|m|/\pi)^{1/4}}{\sqrt{2^{l-|m|}(l-|m|)!}} H_{l-|m|}(\sqrt{|m|}(\theta - \pi/2)) \times e^{-\frac{|m|(\theta-\pi/2)^2}{2}} e^{-im\varphi}\mathbf{e}_z, \tag{D5}$$

where $H_q(z)$ denotes the Hermite polynomials of the degree q. Writing $\theta = \pi/2 + \delta\theta/\sqrt{l_b}$ and $\varphi = \delta\varphi/m_r$ with small angles $\delta\theta$ and $\delta\varphi$, we have the approximations

$$\Theta_{l_b,m_b}(\theta) \approx \sqrt{l_b/\pi}[1 - (\delta\theta)^2], \tag{D6a}$$

$$\Theta_{l_r,m_r}(\theta) \approx \sqrt{m_r/(64\pi)}[1 - (3m_r/l_b)(\delta\theta)^2], \tag{D6b}$$

$$\cos^2 m_r\varphi \approx 1 - (\delta\varphi)^2. \tag{D6c}$$

Following the approach of the separation of variables, we substitute $\psi(\mathbf{r}) = \psi_\rho(\rho)\psi_\theta(\delta\theta)\psi_\varphi(\delta\varphi)$ and $E = E_\rho + E_\theta + E_\varphi$ into the Schrödinger equation (D4) and obtain

$$\left[-\frac{\hbar^2}{2M}\left(\frac{\partial^2}{\partial\rho^2} + \frac{2}{\rho}\frac{\partial}{\partial\rho}\right) + U_\rho(\rho)\right]\psi_\rho(\rho) = E_\rho\psi_\rho(\rho), \tag{D7a}$$

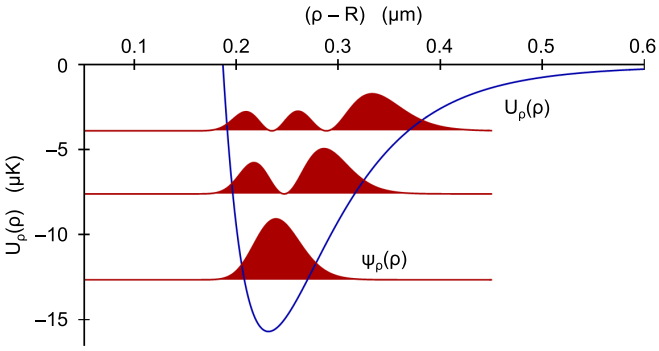

FIG. 5. Vibrational states in the radial potential with the trapping beam powers of $P_b = 3$ W and $P_r = 0.5$ W.

$$\left[-\frac{\hbar^2}{2M}l_b\frac{\partial^2}{\partial(\rho_0\delta\theta)^2} + U_\theta(\rho_0)(\delta\theta)^2\right]\psi_\theta(\delta\theta) = E_\theta\psi_\theta(\delta\theta), \tag{D7b}$$

$$\left[-\frac{\hbar^2}{2M}m_r^2\frac{\partial^2}{\partial(\rho_0\delta\varphi)^2} + U_\varphi(\rho_0)(\delta\varphi)^2\right]\psi_\varphi(\delta\varphi) = E_\varphi\psi_\varphi(\delta\varphi), \tag{D7c}$$

with three potential components

$$U_\rho(\rho) = -\frac{\alpha_b A_b^2}{4}\sqrt{\frac{l_b}{\pi}}\frac{\xi_{l_b}^2(k_b\rho)}{(k_b\rho)^2} - \alpha_r A_r^2\sqrt{\frac{m_r}{64}}\frac{\xi_{l_r}^2(k_r\rho)}{(k_r\rho)^2} - \frac{C_3}{(\rho - R)^3}, \tag{D8a}$$

$$U_\theta(\rho_0) = \frac{\alpha_b A_b^2}{4}\sqrt{\frac{l_b}{\pi}}\frac{\xi_{l_b}^2(k_b\rho_0)}{(k_b\rho_0)^2} + \alpha_r A_r^2\sqrt{\frac{m_r}{64\pi}}\frac{3m_r}{l_b}\frac{\xi_{l_r}^2(k_r\rho_0)}{(k_r\rho_0)^2}, \tag{D8b}$$

$$U_\varphi(\rho_0) = \alpha_r A_r^2\sqrt{\frac{m_r}{64\pi}}\frac{\xi_{l_r}^2(k_r\rho_0)}{(k_r\rho_0)^2}. \tag{D8c}$$

Here, we defined $A_b = A^{(\rm o)}_{n_b,l_b,m_b}$ and $A_r = A^{(\rm o)}_{n_r,l_r,m_r}$. The radial wave function $\psi_\rho(\rho)$ can be solved in a numerical way while $\psi_\theta(\delta\theta)$ and $\psi_\varphi(\delta\varphi)$ behave similarly to a quantum harmonic oscillator.

Setting $P_b = 3$ W and $P_r = 0.5$ W, we obtain a three-dimensional potential well with a depth of about 16 μK, large enough for trapping ultracold Sr spins [35]. The distance from the microsphere's surface to the potential-well minimum is $(\rho_0 - R) = 230$ nm with the distance ρ_0 between the microsphere's center and the potential well (see Fig. 5). In the x-y plane, the trapping potential presents a ring-shaped lattice pattern and the number of lattice sites is $2m_r = 432$. Solving Eq. (D7), we may derive the ground vibrational state whose characteristic frequencies are $(\Omega_\rho, \Omega_\theta, \Omega_\varphi) = 2\pi \times (105, 11, 110)$ kHz along the radial, polar, and azimuthal directions, respectively. The corresponding characteristic lengths are computed as $(\xi_\rho = \sqrt{\frac{\hbar}{M\Omega_\rho}}, \xi_\theta = \sqrt{\frac{\hbar}{M\Omega_\rho}}, \xi_\theta = \sqrt{\frac{\hbar}{M\Omega_\varphi}}) = (33, 104, 32)$ nm. In addition, at $(\rho_0, \theta = \pi/2, \varphi = 0)$, the local intensity of the

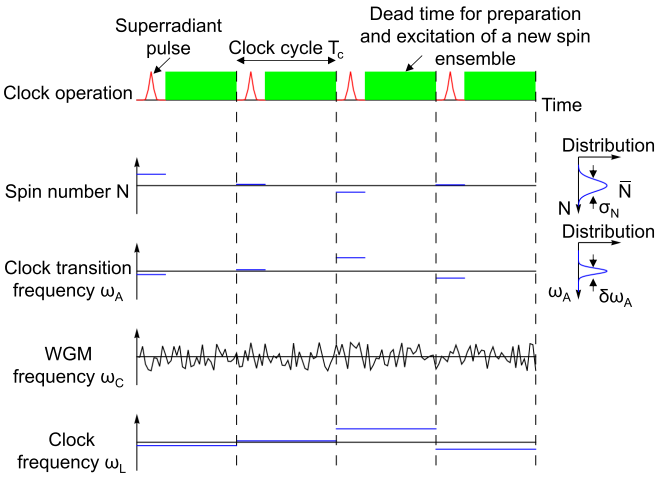

FIG. 6. Schematic diagram of clock operation. Each cycle includes a superradiant pulse and the dead time for preparing and exciting a new spin ensemble. The spin number N follows the Gaussian distribution with a mean value $\bar{N}$ and a standard deviation σ_A. The light shift of the clock transition also follows the Gaussian distribution with a standard deviation $\delta\omega_A$. The fluctuations of the clock WGM frequency ω_C are generated according to the noise spectrum $S_C(f) = h_{C,0}f^0 + h_{C,-2}f^{-2}$.

blue-detuned trapping beam is 11 kW/cm^2, leading to a light shift of $\Delta\nu(\lambda_b) = 2.4$ kHz. Assuming the uncertainty of the trapping-beam intensity to be $\sim$10%, the corresponding uncertainty of $\Delta\nu(\lambda_b)$ is about 0.2 kHz. In contrast, the local intensity of the red-detuned standing wave is 37 kW/cm^2, resulting in $\Delta\nu(\lambda_r) = -1.9$ kHz. The uncertainty of the standing-wave intensity of $\sim$10% gives an uncertainty of $\Delta\nu(\lambda_r)$ of about 0.2 kHz. Moreover, the small difference between $C_3(|\uparrow\rangle)$ and $C_3(|\downarrow\rangle)$ leads to an extra frequency shift $\Delta\nu_{\mathrm{vdW}} = \frac{C_3(|\uparrow\rangle)-C_3(|\downarrow\rangle)}{h(\rho_0-R)^3} = 1.5$ kHz. The uncertainty ξ_ρ gives rise to an uncertainty $\frac{3\xi_\rho}{(\rho_0-R)}\frac{C_3(|\uparrow\rangle)-C_3(|\downarrow\rangle)}{h(\rho_0-R)^3} = 0.3$ kHz of $\Delta\nu_{\mathrm{vdW}}$. Thus, the ring-shaped lattice potential induces a total uncertainty of $(\delta\omega_A/2\pi) = 735$ Hz to the clock transition frequency.

APPENDIX E: CLOCK OPERATION

The clock operation scheme is illustrated in Fig. 6. Each clock cycle with a duration T_c includes one superradiant pulse and the dead time for preparation (i.e., cooling and trapping) and the excitation of a new spin ensemble. The integration time of the photodetector is chosen as 0.1 s, long enough to measure the entire superradiant pulse. The number N of trapped spins varies for different clock cycles and follows the Gaussian distribution with the mean value $\bar{N} = 400$ and the standard deviation $\sigma_N = 40$. In addition, the lattice-induced light shifts introduce an uncertainty of the clock transition frequency ω_A. We model it as a Gaussian distribution with a mean value of $2\pi \times 2$ kHz and a standard deviation $\delta\omega_A = 2\pi \times 0.7$ kHz. In numerical simulation, one may generate N and ω_A for each cycle. Moreover, we numerically produce the frequency ω_C of the noise-perturbed clock WGM based on the spectrum $S_C(f) = h_{C,0}f^0 + h_{C,-2}f^{-2}$ with $h_{C,0} = 2.0 \times 10^{-24}$ s and $h_{C,-2} = 2.0 \times 10^{-22}$ s^{-1}. It should be noted that the frequency ω_C fluctuates throughout the entire clock operation (including multiple cycles). For each cycle, the spectrum $S(\omega)$ of the corresponding superradiant pulse is computed through the master equation and the quantum regression theorem, and then the central frequency ω_L is determined accordingly. Finally, the Allan deviation of the ω_L sequence is evaluated.

[1] C. W. Chou, D. B. Hume, J. C. J. Koelemeij, D. J. Wineland, and T. Rosenband, Phys. Rev. Lett. **104**, 070802 (2010).

[2] B. J. Bloom, T. L. Nicholson, J. R. Williams, S. L. Campbell, M. Bishof, X. Zhang, W. Zhang, S. L. Bromley, and J. Ye, Nature (London) **506**, 71 (2014).

[3] I. Ushijima, M. Takamoto, M. Das, T. Ohkubo, and H. Katori, Nat. Photonics **9**, 185 (2015).

[4] N. Horiuchi, Nat. Photonics **16**, 4 (2022).

[5] M. Takamoto, Y. Tanaka, and H. Katori, Appl. Phys. Lett. **120**, 140502 (2022).

[6] S. B. Koller, J. Grotti, St. Vogt, A. Al-Masoudi, S. Dörscher, S. Häfner, U. Sterr, and Ch. Lisdat, Phys. Rev. Lett. **118**, 073601 (2017).

[7] M. Takamoto, I. Ushijima, N. Ohmae, T. Yahagi, K. Kokado, H. Shinkai, and H. Katori, Nat. Photonics **14**, 411 (2020).

[8] K. W. Martin, G. Phelps, N. D. Lemke, M. S. Bigelow, B. Stuhl, M. Wojcik, M. Holt, I. Coddington, M. W. Bishop, and J. H. Burke, Phys. Rev. Appl. **9**, 014019 (2018).

[9] P. Del'Haye, A. Schliesser, O. Arcizet, T. Wilken, R. Holzwarth, and T. J. Kippenberg, Nature (London) **450**, 1214 (2007).

[10] Z. L. Newman *et al.*, Optica **6**, 680 (2019).

[11] M. A. Norcia, J. R. K. Cline, J. A. Muniz, J. M. Robinson, R. B. Hutson, A. Goban, G. E. Marti, J. Ye, and J. K. Thompson, Phys. Rev. X **8**, 021036 (2018).

[12] J. Chen, Active optical clock, Chin. Sci. Bull. **54**, 348 (2009).

[13] M. L. Gorodetsky, A. A. Savchenkov, and V. S. Ilchenko, Opt. Lett. **21**, 453 (1996).

[14] D. W. Vernooy, V. S. Ilchenko, H. Mabuchi, E. W. Streed, and H. J. Kimble, Opt. Lett. **23**, 247 (1998).

[15] D. K. Armani, T. J. Kippenberg, S. M. Spillane, and K. J. Vahala, Nature (London) **421**, 925 (2003).

[16] S. Balac, Comput. Phys. Commun. **243**, 121 (2019).

[17] F. Vollmer and D. Yu, *Optical Whispering Gallery Modes for Biosensing: From Physical Principles to Applications* (Springer International Publishing, New York, 2020).

[18] D. Yu and F. Vollmer, Phys. Rev. Res. **3**, 023087 (2021).

[19] D. Yu, M. Humar, K. Meserve, R. C. Bailey, S. Nic Chormaic, and F. Vollmer, Nat. Rev. Methods Primers **1**, 83 (2021).

[20] T. J. Kippenberg, S. M. Spillane, and K. J. Vahala, Phys. Rev. Lett. **93**, 083904 (2004).

[21] D. Yu and F. Vollmer, Commun. Phys. **4**, 77 (2021).

[22] B. Peng, Ş. K. Özdemir, F. Lei, F. Monifi, M. Gianfreda, G. L. Long, S. Fan, F. Nori, C. M. Bender, and L. Yang, Nat. Phys. **10**, 394 (2014).
[23] W. Chen, Ş. K. Özdemir, G. Zhao, J. Wiersig, and L. Yang, Nature (London) **548**, 192 (2017).
[24] A. Schliesser, R. Rivière, G. Anetsberger, O. Arcizet, and T. J. Kippenberg, Nat. Phys. **4**, 415 (2008).
[25] A. Schliesser, O. Arcizet, R. Rivière, G. Anetsberger, and T. J. Kippenberg, Nat. Phys. **5**, 509 (2009).
[26] D. Yu and F. Vollmer, Active optomechanics, Commun. Phys. **5**, 61 (2022).
[27] T. Aoki, B. Dayan, E. Wilcut, W. P. Bowen, A. S. Parkins, T. J. Kippenberg, K. J. Vahala, and H. J. Kimble, Nature (London) **443**, 671 (2006).
[28] C. Junge, D. O'Shea, J. Volz, and A. Rauschenbeutel, Phys. Rev. Lett. **110**, 213604 (2013).
[29] E. Will, L. Masters, A. Rauschenbeutel, M. Scheucher, and J. Volz, Phys. Rev. Lett. **126**, 233602 (2021).
[30] D. Yu and F. Vollmer, Sci. Rep. **11**, 13899 (2021).
[31] D. Yu, F. Vollmer, and S. Zhang, Quantum Sci. Technol. **8**, 025005 (2023).
[32] D. Yu, F. Vollmer, P. Del'Haye, and S. Zhang, Opt. Express **31**, 6228 (2023).
[33] M. Takamoto, H. Katori, S. I. Marmo, V. D. Ovsiannikov, and V. G. Pal'chikov, Phys. Rev. Lett. **102**, 063002 (2009).
[34] M. Takamoto, F.-L. Hong, R. Higashi, and H. Katori, Nature (London) **435**, 321 (2005).
[35] H. Katori, T. Ido, Y. Isoya, and M. Kuwata-Gonokami, Phys. Rev. Lett. **82**, 1116 (1999).
[36] A. D. Ludlow, M. M. Boyd, T. Zelevinsky, S. M. Foreman, S. Blatt, M. Notcutt, T. Ido, and J. Ye, Phys. Rev. Lett. **96**, 033003 (2006).
[37] M. O. Scully, E. S. Fry, C. H. R. Ooi, and K. Wódkiewicz, Phys. Rev. Lett. **96**, 010501 (2006).
[38] S. Okaba, D. Yu, L. Vincetti, F. Benabid, and H. Katori, Commun. Phys. **2**, 136 (2019).
[39] D. Meiser, J. Ye, D. R. Carlson, and M. J. Holland, Phys. Rev. Lett. **102**, 163601 (2009).
[40] D. Yu, J. Opt. Soc. Am. B **33**, 797 (2016).
[41] T. Bothwell, C. J. Kennedy, A. Aeppli, D. Kedar, J. M. Robinson, E. Oelker, A. Staron, and J. Ye, Nature (London) **602**, 420 (2022).
[42] X. Zheng, J. Dolde, V. Lochab, B. N. Merriman, H. Li, and S. Kolkowitz, Nature (London) **602**, 425 (2022).
[43] I. Ushijima, M. Takamoto, and H. Katori, Phys. Rev. Lett. **121**, 263202 (2018).
[44] A. Aeppli, A. Chu, T. Bothwell, C. J. Kennedy, D. Kedar, P. He, A. M. Rey, and J. Ye, Sci. Adv. **8**, eadc9242 (2022).
[45] M. Cai, O. Painter, and K. J. Vahala, Phys. Rev. Lett. **85**, 74 (2000).
[46] M. A. Norcia, R. J. Lewis-Swan, J. R. K. Cline, B. Zhu, A. M. Rey, and J. K. Thompson, Science **361**, 259 (2018).
[47] R. H. Dicke, Phys. Rev. **93**, 99 (1954).
[48] R. Friedberg and J. T. Manassah, Laser Phys. Lett. **4**, 900 (2007).
[49] M. A. Norcia, M. N. Winchester, J. R. K. Cline, and J. K. Thompson, Sci. Adv. **2**, e1601231 (2016).
[50] T. Laske, H. Winter, and A. Hemmerich, Phys. Rev. Lett. **123**, 103601 (2019).
[51] A. Cidrim, A. Piñeiro Orioli, C. Sanner, R. B. Hutson, J. Ye, R. Bachelard, and A. M. Rey, Phys. Rev. Lett. **127**, 013401 (2021).
[52] M. L. Gorodetsky and I. S. Grudinin, J. Opt. Soc. Am. B **21**, 697 (2004).
[53] D. Yu and R. Dumke, Phys. Rev. A **100**, 022124 (2019).
[54] G. Santarelli, C. Audoin, A. Makdissi, P. Laurent, G. J. Dick, and A. Clairon, IEEE Trans. Ultrason. Ferroelectr. Freq. Control **45**, 887 (1998).
[55] C. C. Lam, P. T. Leung, and K. Young, J. Opt. Soc. Am. B **9**, 1585 (1992).
[56] I. H. Malitson, Interspecimen comparison of the refractive index of fused silica, J. Opt. Soc. Am. **55**, 1205 (1965).
[57] W. Blanc and B. Dussardier, J. Opt. **45**, 247 (2016).
[58] H. Katori, M. Takamoto, V. G. Pal'chikov, and V. D. Ovsiannikov, Phys. Rev. Lett. **91**, 173005 (2003).
[59] X. Zhou, X. Xu, X. Chen, and J. Chen, Phys. Rev. A **81**, 012115 (2010).
[60] F. Le Kien, V. I. Balykin, and K. Hakuta, Phys. Rev. A **70**, 063403 (2004).